Activation of the influenza B M2 proton channel (BM2)

Zhi Yue, Jiangbo Wu, Da Teng, Zhi Wang,[†] and Gregory A. Voth[*]

Department of Chemistry, Chicago Center for Theoretical Chemistry, James Frank Institute, and Institute for Biophysical Dynamics, The University of Chicago, Chicago, Illinois 60637, USA

[†]Present address: HAKUHODO Technologies Inc., Minato, Tokyo, 107-6320, Japan.

[*]Corresponding to: Gregory A. Voth, gavoth@uchicago.edu

Running title: *pH-dependent conformational activation of BM2*

Keywords: influenza virus, ion channel, channel activation, proton transport, membrane protein, protein conformation, conformational change, computer modeling, molecular dynamics

Abstract

Influenza B viruses have co-circulated during most seasonal flu epidemics and can cause significant human morbidity and mortality due to their rapid mutation, emerging drug resistance, and severe impact on vulnerable populations. The influenza B M2 proton channel (BM2) plays an essential role in viral replication, but the mechanisms behind its symmetric proton conductance and the involvement of a second histidine (His27) cluster remain unclear. Here we perform the membrane-enabled continuous constant-pH molecular dynamics simulations on wildtype BM2 and a key H27A mutant to explore its pH-dependent conformational switch. Simulations capture the activation as the first histidine (His19) protonates and reveal the transition at lower pH values compared to AM2 is a result of electrostatic repulsions between His19 and pre-protonated His27. Crucially, we provide an atomic-level understanding of the symmetric proton conduction by identifying pre-activating channel hydration in the C-terminal portion. This research advances our understanding of the function of BM2 function and lays the groundwork for further chemically reactive modeling of the explicit proton transport process as well as possible anti-flu drug design efforts.

Introduction

Influenza A and B viruses pose severe global health threats to humans due to their high mutation rates, emerging drug resistance, and cross-species transmission, particularly between Influenza A viruses and avian influenza (bird flu).(1, 2) Viroporins are small ion channels that facilitate virus release from infected host cells by enhancing the passive transport of ions and small molecules through the membrane, making them ideal targets for antiviral therapeutics (3-5). The matrix 2 proteins of influenza A virus (AM2) (6) and influenza B virus (BM2) (7) are proton-selective (8-16) ion channels (12, 17). Both channels are essential for viral replication (18-20) because acidifying the virion interior by proton influx through the channel is a prerequisite for releasing the virus genetic material into the host cell (21, 22).

Both channels are homotetramers (23, 24) that adopt an N_{out}/C_{in} orientation in membranes (25, 26) (Fig. 1*AB*) but share little sequence homology except for an HxxxW motif (His37 and Trp41 in AM2, His19 and Trp23 in BM2, Fig. 1*C*) in the transmembrane domain. Crystallography and NMR spectroscopy have determined the closed and open structures of both channels (Table S1). In the closed-state, AM2 and BM2 pores are occluded by Val27 and Phe5 at the N-terminal (NT) side but are wide enough for water diffusion until reaching His19 and His37, respectively (Fig. 1*AB*). The presence of water in the NT-half of a closed pore, which is assumed to be a requirement for proton conductance (27), is supported by experiment (28, 29) and simulation (13-16, 29-36). It

should be noted that of these numerous simulation papers only two (13, 14) have calculated the explicit channel proton conductance and activation process, and both for AM2 but not BM2. The other simulation papers have generally inferred or assumed these behaviors from looking at water within the channel and channel conformational changes, but not by also including proton transport via an explicit excess proton (or protons) in the channel and with Grotthuss proton shuttling occurring in the underlying molecular dynamics (MD) modeling algorithm.

The pores constrict at His37 in AM2 or His19 in BM2 (Fig. 1*AB*) and are respectively interrupted by densely packed Trp41 or Trp23. The pores widen after Trp41 in AM2 or Trp23 in BM2 (Fig. 1*AB*). Asp44 and Arg45 in AM2 define the C-terminal (CT) end of the pore (Fig. 1*A*), while in BM2, the pore ends correspondingly at Gly26 and a second histidine His27 (Fig. 1*B*).

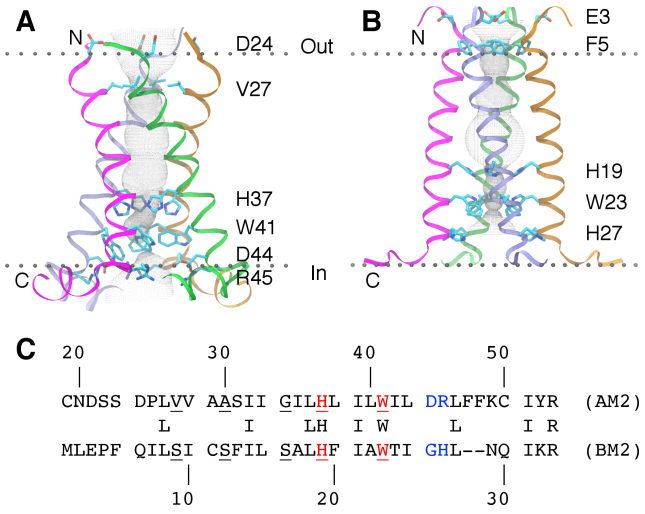

Figure 1. Structures and sequences of M2 proteins. Closed-state structures and crucial residues for AM2 (*A*) and BM2 (*B*). M2 tetramers (PDB IDs: 2L0J (37) and 6PVR (38) for AM2 and BM2, respectively) are shown as ribbons (ice-blue, orange, green, and magenta for chains a, b, c, and d, respectively). Residues are displayed as sticks. A gray mesh depicts the pores calculated using HOLE (39). Black dots depict the lipid head groups computed by the Positioning of Proteins in Membranes (40) (PPM) server. Membrane orientation and M2 termini are labeled. (*C*) Sequence alignment of AM2 and BM2 (UniProtKB accession numbers: P0DOF5 and B4UQM4, respectively) using the Basic Local Alignment Search Tool (41) (BLAST). Pore-lining residues are underlined. HxxxW motifs are highlighted in red. Asp44 and Arg45 in AM2, and Gly26 and His27 in BM2 are highlighted in blue.

In AM2, His37 is essential for the channel activity and H^+ selectivity. Replacing His37 with Gly, Glu, Ser, or Thr removes the pH-dependent H^+ conduction and makes the channel permeable to Na^+ and K^+ (42, 43). As the pH reduces in the wildtype (WT) channel, the net charge of the His37 tetrad increases from +0 to +4. AM2 activates around pH 6 (8, 10, 42, 44), where the His37 tetrad cycles between charge states of +2 and +3 based on experimental pK_as (45, 46). Upon activation, electrostatic repulsion between charged His37 residues widens the pore and opens the Trp41 gate (likely through cation–π interactions (13, 47)) for H^+ influx (13, 14, 37, 48, 49). In addition to simulations involving explicit proton transport (13, 14), pore opening induced by charging His37 from +2 to +3 has also been captured by fixed-protonation-state (29, 30, 32, 33) (FPS) and continuous constant-pH molecular dynamics (50, 51) (CpHMD) simulations. However, it has sometime been debated if His37 is directly involved in the proton transport (PT). A "shutter" mechanism suggests that protons diffuse through a continuously hydrated open pore without changing the charge state of His37 (30, 47), while a "shuttle" mechanism argues that His37 shuttles the proton through the His37/Trp41 "bottleneck" via local conformational switch coupled with the

protonation (37, 46, 48, 49, 52). Using multiscale reactive molecular dynamics (53-56) (MS-RMD) and quantum mechanics/molecular mechanics (57-59) (QM/MM) simulations, Voth and co-workers have modeled the permeation of an explicit proton through AM2 and confirmed proton "shuttling" through His37 (13-16). Trp41 also regulates the asymmetric conductance, i.e., much greater H^+ influx when $pH_{out} < pH_{in}$ than H^+ efflux when $pH_{out} > pH_{in}$ (60, 61). W41A, W41C, and W41F mutations lead to large H^+ efflux (62). Asp44 is not strictly conserved and some naturally occurring variants have an Asn at this position (63). Mutations to Asn, Gly, Ala, Thr, Lys, and Phe make the channel more conductive (60, 64-66). Asp44 is hydrogen-bonded (HBonded) with W41 in the closed state (28, 29), and Asp44 substitutions enhance H^+ flux by destabilizing the closed Trp41 gate (66). Asp44 also contributes to the asymmetric flux as the Cys, Ala, and Asn replacements dramatically increase H^+ efflux when $pH_{out} > pH_{in}$ (66). MS-RMD and QM/MM simulations have shown that the D44N mutation reduces the free energy barrier of PT between His37 and the viral interior, facilitating H^+ efflux (67). Arg45 ion-pairs with Asp44 (28, 29) but has not been confirmed as essential for asymmetric conduction; H^+ conduction through the R45C mutant remains asymmetric (66).

The BM2 channel displays a similar pH-dependent acidification profile (12) but differs from AM2 in several ways. First, BM2 activates and saturates at lower pH values (68). Second, BM2 has a higher activity or PT rate (68, 69). Third, the proton conductance through BM2 is symmetric, i.e., there is non-negligible H^+ efflux when $pH_{out} > pH_{in}$ (12, 68). Last, BM2 is insensitive to antiviral drugs amantadine (12) and rimantadine (69). In analogy to His37 in AM2, His19 is an irreplaceable pH sensor in BM2 and replacements with Cys, Ala, and Leu disrupt channel activity (12, 70-72). Trp23 is also essential to BM2 functions (70), but it has been suggested that interactions between His19 and Trp23 in BM2 differ those between His37 and Trp41 in AM2 (71). Mutants W23C and W23F are not H^+ selective (12, 72), indicating that Trp23 is the H^+ selectivity filter. His27 presents the most prominent structural difference in BM2. The channel activity is only partially impaired by the H27A substitution (69, 72). Replacing His27 with Arg (the AM2 equivalence) has little impact on H^+ efflux, but mutating Gly26 to Asp (the AM2 equivalence) reduces it (68). The G26D/H27R double mutant is AM2-like and exhibits no H^+ efflux (68), indicating that His27 is a key regulator of symmetric conductance.

Despite the electrophysiological progress, the activation mechanism of BM2 remains elusive. FPS MD simulations have suggested that the pore opens when His19 becomes triply or fully protonated (73-75). This is supported by the closed and open structures respectively solved at pH 7.5 and 4.5 (38), along with the experimental pK_as of His19 and His27 (76, 77). Gelenter et al. have combined NMR and FPS MD simulations to study the dynamics of water molecules in the channel under charge states $H19^0/H27^{+1}$ and $H19^{+4}/H27^{+4}$, and revealed that the higher mobility of water molecules in the open channel enables an HBonded water wire for H^+ conduction (36). Note that the chosen charge states represent two extremes of the activation profile, so information from the transition region has not been collected. Zhang et al. have explored a broader pH range using discrete constant-pH molecular dynamics and found that activation may be triggered by the triple-protonation of the His19 tetrad (78). However, the membrane environment has not been taken into account by their employed implicit solvent generalized Born (GB) model when updating the charge states using a Monte Carlo approach. The absence of a membrane representation in the GB model, i.e., placing BM2 in a water environment, complicates the rigor of the charge-state sampling and the coupled conformational dynamics.

Here, we employed the membrane-enabled (50) hybrid-solvent (79) CpHMD technique to understand the activation of BM2 over a wide pH range. We sought to answer the following questions: (1) How does BM2 activate in response to pH reduction; and (2) how does His27 impact the channel dynamics? We confirm that BM2 opens when His19 becomes triply protonated. In

addition, we observe that His27 pushes channel activation to lower pH values and increases channel hydration in the CT-portion before activation, which explains the atomistic origin of symmetric H^+ conduction in BM2. The present work yields new insights into BM2 activation and paves the way for further investigation of the PT process (13, 14) using explicitly reactive proton transport simulations (53-56).

Results and Discussion

Progressive protonation of His19 and His27 tetrads

We first examined the pK_as of the protonatable residues. Microscopic pK_as assuming independent protonation were calculated for Glu3 using the Hill equation (80) (Eq. S1 of Supporting Information). For interacting residues with coupled protonation such as His19 and His27 (76, 77, 81), a four-proton model (50) (Eq. S2) was used to compute stepwise pK_1/pK_2/pK_3/pK_4. The time series of pK_a (Fig. S1) and the unprotonated fraction (S^{unprot}, Figs. S2–S3) indicate convergence beyond 40 ns for all pH replicas. We thus used the 40–100 ns for analysis.

The WT simulation yields stepwise pK_as of 6.9, 6.0, 5.4, and 4.7 for His19 (Fig. 2*AD*), indicating that the tetrad stepwise stays neutral (P_0, red line in Fig. 2*A*) at pH > 6.9, then binds the first (P_1, orange line) and second (P_2, brown line) protons in a pH range of 6.9–6 and 6–5.4, respectively. The triply protonated state (P_3, green line) emerges at pH 5.4 and dominates until pH 4.7, where His19 becomes fully protonated (P_4, blue line). The calculated pK_as are somewhat higher by < 1 pH unit than those obtained by Hong and co-workers using solid-state NMR (ssNMR) (76) (Fig. 2*D*). The dominant charge states of the His27 tetrad are P_0, P_1, P_2, P_3, and P_4 in pH ranges of > 7.5, 7.5–6.9, 6.9–6.2, 6.2–5.3, and < 5.3, respectively (Fig. 2*BD*). Compared to the ssNMR values (77) (Fig. 2*D*), the calculated values are smaller for pK_1/pK_4 but higher for pK_2/pK_3 by ≤ 1 pH unit. The simulated sequence of protonation is $H19^0/H27^{+1}$ → $H19^{+1}/H27^{+2}$ → $H19^{+1}/H27^{+3}$ → $H19^{+2}/H27^{+3}$ → $H19^{+3}/H27^{+3}$ → $H19^{+3}/H27^{+4}$ → $H19^{+4}/H27^{+4}$, while the experimental sequence is $H19^0/H27^{+1}$ → $H19^{+1}/H27^{+1}$ → $H19^{+1}/H27^{+3}$ → $H19^{+1}/H27^{+4}$ → $H19^{+2}/H27^{+4}$ → $H19^{+3}/H27^{+4}$ → $H19^{+4}/H27^{+4}$. The major differences are 1) the simulated protonation pH range (7.5–4.7) is narrower than the experimental range (7.9–4.2), and 2) the His19 tetrad cycles between charge states P_2 and P_3 when His27 is triply protonated in the simulation but fully protonated in the experiment. However, the simulated pK_as of His19 are consistently smaller than those of His27, which agrees with the experiments (76, 77). The H27A mutant simulation yields stepwise pK_as of 7.0, 6.1, 5.3, and 4.6 for His19 (Fig. 2*CD*), which equal the WT values. However, the His19 protonation pH range widens to 2.4 from the WT's 2.2, which coincides with experiments (3.6 vs. 1.9) albeit to a smaller extent.

The origin of the discrepancies in pK_as is likely twofold. First, the GB model underlying the CpHMD underestimates desolvation (79), especially for deeply buried residues (82), leading to underestimated histidine pK_a shifts due to their electrostatic repulsions (79) and a narrower protonation pH range (50). Second, our simulations at 308 K used a POPC (1-palmitoyl-2-oleoyl-*sn*-glycero-3-phosphocholine) membrane while the ssNMR experiments at 243–263 K employed a virus-mimetic (VM+; POPC:POPE:sphingomyelin:cholesterol with a molar ratio of 1:1:1:1) membrane (76, 77). Under experimental conditions, BM2 is expected to be more compact and less flexible (as discussed in the subsequent section), and repulsions between histidines are reinforced, resulting in a larger pK_a differences and a wider protonation pH range.

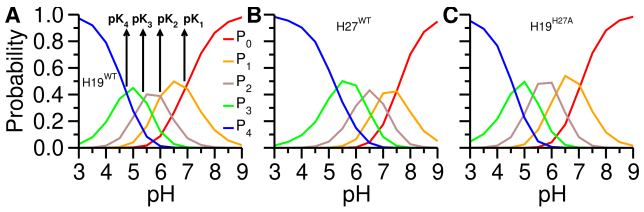

D

	WT				H27A	
	H19		H27		H19	
	Expt.	Calc.	Expt.	Calc.	Expt.	Calc.
pK_1	6.1±0.1	6.9±0.1	7.9±0.1	7.5±0.1	7.8±0.3	7.0±0.1
pK_2	5.7±0.1	6.0±0.1	5.9±0.1	6.9±0.0	5.2±0.2	6.1±0.0
pK_3	4.5±0.3	5.4±0.1	5.9±0.1	6.2±0.1	5.2±0.2	5.3±0.1
pK_4	4.2±0.4	4.7±0.1	5.8±0.1	5.3±0.0	4.2±0.4	4.6±0.1

Figure 2. Titration of the His tetrads. Stepwise protonation of the wildtype (WT) His19 (*A*), His27 (*B*), and the H27A mutant His19 (*C*). P_0, P_1, P_2, P_3, and P_4 represent the probabilities of binding 0 (red), 1 (orange), 2 (brown), 3 (green), and 4 (blue) protons, respectively. Stepwise $pK_1/pK_2/pK_3/pK_4$ are intercepts of adjacent population curves and are indicated by arrows. (*D*) Stepwise pK_as calculated using Eqs. S1–S2. The reported means and errors (standard deviations) were estimated from block analysis (block values are given in Table S6). Experimental data were taken from Hong and co-workers (76, 77, 81).

Chen et al. studied AM2 using the CpHMD and reported stepwise pK_as of 8.3/7.1/6.2/5.7 for His37 (50), which are larger than those for His19 in BM2 by 1 pH unit or more. This raises a question: why does the histidine protonate at lower pH values in BM2? We measured the minimum distances between histidines versus pH. At pH ≥ 6 where the His19 tetrad is singly protonated or neutral, His19 residues are in close contact (a major peak at 4 Å, Fig. S4*A*). At pH ≤ 5.5 where the tetrad starts to bind more protons, the residues become separated (a second peak centers around 7 Å starts to dominate, Fig. S4*A*). This is expected given the increasing electrostatic repulsions as the charge accumulates. The separation displays a similar pH dependence in the absence of His27 (Fig. S5). The separation between His19 and His27 does not show strong pH dependence (one peak centers around 7–8 Å, Fig. S4*C*), which is not surprising based on the same-helix positioning of His19 and His27. To better assess the impact of His27, we investigated the correlation between the charge states of the His19 tetrad and that of the closest His27 residue at pH 5.5. As plotted in Fig. S4*D*, the tetrad samples more states P_1 and P_2 with the closest His27 residue charged but favors states P_3 and P_4 when the His27 is neutral. This anticorrelation (reduced repulsions with His27 favors proton binding to His19) explains the downshifted protonation region of BM2 His19 relative to that of AM2 His37.

BM2 activates at a lower pH with a narrower transition region

We then investigated the pH-induced conformational changes of BM2. The AM2 CpHMD study revealed two well separated populations of the backbone root-mean-squared deviation (RMSD) with pH-dependent relative weights (50). However, we were unable to identify a clear pH dependence in the RMSD for BM2. The RMSD profiles display either a non-monotonic trend (WT, Fig. S6*A*) or multiple overlapping populations (H27A, Fig. S6*B*). Thus, we monitored the pore dimension along the channel axis using the quadrilateral perimeter of the pore-lining residues Phe5, Leu8, Ser12, Ser16, His19, Trp23, and His27, which is the boundary length of a polygon connecting the four C_α atoms. ssNMR captures changes in the perimeter of 28.3, 14.0, 9.6, 6.2, 6.2, 0.8, and –5.6 Å for Phe5, Leu8, Ser12, Ser16, His19, Trp23, and His27, respectively, when going from the closed (PDB ID: 6PVR) to the open (PDB ID: 6PVT) state (Table S2). This indicates that BM2 undergoes a rigid scissor motion with the hinge at Trp23 upon activation in the experiment (38). While in our simulation, all perimeters except at Phe5 rapidly increase as the pH reduces from 6.5 to 4.5 (Fig. 3*A*). The closer to the CT, the larger the increase (4.0, 4.2, 5.8, 7.1, 10.0, and 12.8 Å

for Leu8, Ser12, Ser16, His19, Trp23, and His27, respectively). The ssNMR structures, determined in rigid gel-phase POPE (1-palmitoyl-2-oleoyl-*sn*-glycero-3-phosphoethanolamine) membranes at 280–290 K, contrast with BM2's dynamics in fluid-phase POPC membranes at 308 K in our simulations.

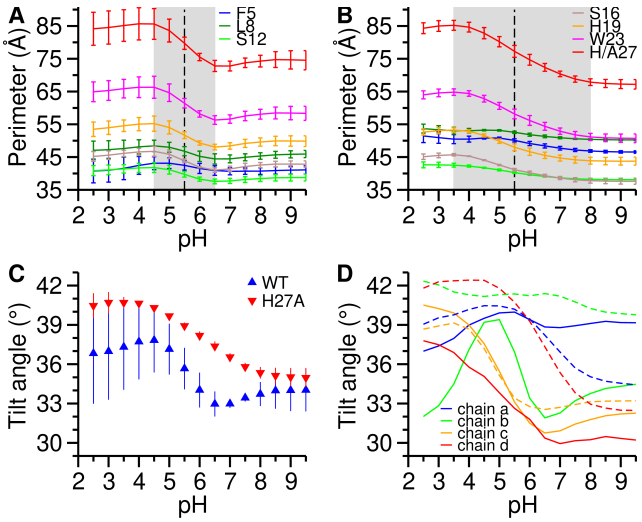

Figure 3. pH-dependent conformational change. Quadrilateral perimeters of the C_α atoms of pore-lining residues in the WT (*A*) and H27A mutant (*B*) simulations. Pore-lining residues include: Phe5 (blue), Leu8 (dark green), Ser12 (green), Ser16 (brown), His19 (orange), Trp23 (magenta), and His/Ala27 (red). Means over the simulation time were plotted versus pH values and errors were standard deviations estimated from block analysis (same below). Gray boxes and vertical black lines mark the transition regions and midpoints, respectively. Midpoints were computed by fitting relative changes to the Hill equation (80) (Eq. S1). A perimeter comparison between the WT and H27A is given in Fig. S7. The distributions are displayed in Figs. S8 (WT) and S9 (H27A). (*C*) Average tilt angle between the C-terminal helices (residues 15–28) and the N-terminal helical bundle (residues 7–14) in the WT (blue up triangle) and H27A mutant (red down triangle). Note that the calculations were insensitive to atom selections (Fig. S14). (*D*) Tilt angle between each C-terminal helix (blue, green, orange, and red for chains a, b, c, and d, respectively) and the N-terminal helical bundle in the WT (solid line) and H27A mutant (dashed line). For clarity, error bars are not shown (displayed in Fig. S15).

To assess the impact of lipid composition on channel behavior, we performed μs-long FPS simulations for the closed ($H19^0/H27^{+1}$) and open ($H19^{+3}/H27^{+4}$) states in POPC and VM+ bilayers at 308 K, and in POPE bilayers at 280 K. Note that VM+ membranes at 308 K are in a fluid phase (83) and POPE membranes at 280 K are in a gel phase (84-87). We did not run VM+ simulations between 243–263 K due to known issues with the TIP3P water model (88, 89) below the freezing point (90). In the FPS simulations with a gel-phase POPE bilayer, it is not surprising that the perimeters of the pore-lining residues stay close to the ssNMR values, despite a relatively constricted pore between Ser12 and Trp23 (Fig. S10). Regarding the fluid-phase simulations, the time series of RMSD indicates that BM2 is more stable in VM+ membranes than in POPC membranes in either the closed (Fig. S11, red vs. orange lines) or open (Fig. S11, blue vs. green lines) states. Consistent with the WT CpHMD simulation, all the perimeters increase upon activation in the FPS simulations with a POPC bilayer (Fig. S12, solid lines), with larger increases observed closer to the CT. By contrast, in the FPS simulations with a VM+ bilayer, the perimeters increase at His19 and above but decrease at His27, while remaining nearly unchanged at Trp23 (Fig. S12, dashed lines). This pattern corresponds with the ssNMR structures and indicates that BM2 undergoes a rigid scissor motion with the hinge at Trp23 in fluid-phase VM+ membranes. This is likely due to the immobilization of BM2 in cholesterol-rich VM+ membranes, which has also been observed for AM2 in VM+ membranes at physiological temperatures using ssNMR (83).

The WT CpHMD simulation shows that the His19 tetrad takes two protons within the transition region pH 6.5–4.5 and oscillates between charge states P_2 and P_3 at the transition midpoint pH 5.5 (Fig. 2*D*). This supports earlier MD simulations (73, 78) and ssNMR experiments (38, 76, 77), confirming BM2 activation upon triple-protonation of His19. Notably, the simulated activation midpoint is lower than that of AM2 (pH 6.0) (50), aligning with electrophysiological observations that BM2 activates at lower pH values (68). The H27A simulation reveals notable variances, with a broader transition region of pH 3.5–8 in the perimeter profiles (Fig. 3*B*). However, the transition midpoint remains the same (Fig. 3*B*). Otomo et al. found that the H27A mutation reduced the maximum H^+ conductance without altering the transition midpoint (72). Despite a 1 pH unit difference between the calculated (5.5) and measured (6.4) midpoints, likely due to the systematic shift caused by the GB mode and different experimental lipid environments, our simulations concur with the experiments regarding the mutant's impact. Like the WT, all mutant perimeters progressively increase as the pH is lowered. But there are sensible differences. Compared to the WT, H27A has a wider pore at Phe5 and Leu8 at all pH values but narrows at Ser16 and below at pH > 4 (Figs. 3*AB* and S7). This is likely due to the absence of electrostatic repulsions between His19 and His27 in the mutant. As the WT channel stays closed (Fig. 3*A*) when His27 protonates (Fig. 2*BD*) at pH > 6.5, it is expected that the CT shrinkage becomes significant at pH > 6.5 in H27A (Fig. S7). The contrasting trends of expansion at the NT and shrinkage at the CT suggest a rigid motion in BM2 helices during activation.

Another feature is the tilt angle between the CT-half helix (residues 7–14 and 25–32 for AM2 and BM2, respectively) and the NT-half helical bundle (residues 15–28 and 33–46 in AM2 and BM2), which has proven useful for probing AM2 activation (91). Like in the AM2 CpHMD simulation (50), the NT helical bundle's tilt relative to the membrane normal is less sensitive to pH in the BM2 simulation (Fig. S13). The average tilt angle between the CT-helices and the NT-bundle slightly increases from around 34º to 37º when BM2 activates at low pH values (Fig. 3*C*, blue up triangles). ssNMR structures record an increase from 20º (PDB ID: 6PVR) to 22º (PDB ID: 6PVT). In contrast, AM2 sees an increase from 21º (PDB ID: 3LBW) to 37º (PDB ID: 3C9J) in crystallography and from 23º to 44º in the CpHMD simulation (50). Our BM2 simulation aligns with these findings, showing a smaller tilt angle increase upon activation compared to AM2. The H27A mutant displays similar behavior but reports a larger CT tilt at low pH values (40º; Fig. 3*C*, red down triangles). Overall trends of tilting agree with the perimeter ones (the same transition region and midpoint). But inspecting tilt angles of each helix show asynchronous tilting in WT (considerable increases in chains c and d as pH reduces, minor decrease in chain a, and a big decrease after an initial increase in chain b; Fig. 3*D*, solid lines), whereas in H27A, tilting is synchronous (a uniform increase across all four chains; Fig. 3*D*, dashed lines).

H27 increases the C-terminal hydration

We now turn to channel hydration and count water molecules along the channel axis (N_{Water}) in both the WT and the H27A mutant. The WT hydration remains unaltered until pH 6.5, then starts to increase at pH 6, where His19 takes the second H^+ (Fig. 2*AD*), and continues rising as the pH further reduces (Fig. S16*A*). The change in hydration varies by location. Going from the closed state at pH 8 ($His19^0$/$His27^0$) to the open state at pH 4 ($His19^{+4}$/$His27^{+4}$), the channel experiences a greater increase in hydration in the CT-half than in the NT-half (Fig. S17*A*), consistent with the perimeter-based channel expansion (Fig. 3*A*). The increase in hydration is pronounced between His27 and Ser16 (–13 Å ≤ Z ≤ 1 Å) and maximizes (6 H_2O molecules) around Trp23 (Z = –7 Å).

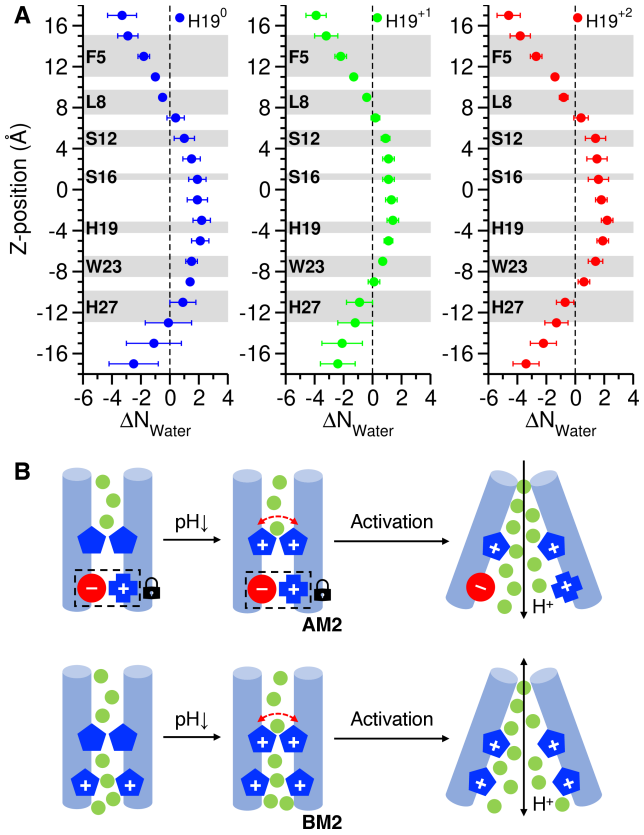

Figure 4. pH-dependent channel hydration. (*A*) Differences in channel hydration between the WT and H27A mutant (ΔN_{Water}) when His19 is neutral (left), singly protonated (middle), and doubly protonated (right). Errors were calculated through error propagation. Gray boxes indicate the side-chain center-of-mass (COM) of the pore-lining residues (centroid and halved box width respectively represent the mean and standard deviation). Vertical dashed lines mark ΔN_{Water} of 0. The COMs were computed using heavy atoms and projected to the channel axis, with the four Ala17 C_α atoms centered at the origin. (*B*) Model depicting proton transport (PT) directionality in AM2 (top) and BM2 (bottom). Blue pentagons, red circles, blue crosses, and green circles represent the M2 histidines, AM2 Asp44, AM2 Arg45, and H_2O, respectively. Red dashed arches denote electrostatic repulsions between protonated AM2 His37 or BM2 His19. In the closed-stat AM2, only the NT-half of the channel is hydrated as Asp44–Arg45 salt-bridges block H_2O accessibility from the CT-entrance, making the PT asymmetric. While in the closed-state BM2, protonated His27 opens the CT-entrance and provides H_2O accessibility, leading to symmetric PT.

The H27A hydration profile displays a similar trend of increasing channel hydration with decreasing pH, particularly in the CT-half between Ala27 and Ser16 (Figs. S16*B* and S17*B*). However, there is a notable difference: the closed WT contains 1–2 more H_2O molecules per 2-Å layer between His27 and Ser12 (-9 Å $\leq Z \leq 3$ Å) than H27A (Fig. 4*A*, left panel). When His19 is singly or doubly protonated, the WT channel also exhibits increased hydration in this region (Fig. 4*A*, middle and right panels). This suggests that His27 contributes to increased hydration in the CT-portion before activation. In AM2, Asp44 and Arg45 (equivalent to BM2's Gly26 and His27) form interhelical salt-bridges in the closed state at high pH values (50), which likely seals the CT-entrance and blocks water entry until His37's triple-protonation from the NT side leads to channel expansion, resulting in asymmetric H^+ conduction. This is supported by MS-RMD simulations of the WT (15) and D44N mutant (67) of AM2, which found increased hydration by about 2 H_2O molecules below Trp41 before His37 becomes triply protonated. The H_2O network altered by the D44N mutation explains the reduced free energy barrier for protonating His37 from the interior (67) and the symmetric H^+ conduction in the mutant (66). While in BM2, lacking such salt-bridges, His27 protonates before His19, drawing water molecules into the channel and enabling H^+ access to His19 from the CT side, explaining the symmetric H^+ conduction in BM2 (Fig. 4*B*). This is

supported by mutagenesis studies: the H27R mutant mimics WT, the G26D mutant reduces the H^+ efflux, and the AM2-like G26D/H27R double mutant blocks it (68). The H^+ efflux is not blocked in the G26D mutant likely because His27 side-chains are not bulky enough to effectively block water entry if ion-paired with Asp26. These findings suggest that the H^+ efflux in M2 proteins requires a precise geometrical side-chain arrangement at the CT-entrance. This result may also present an opportunity for a drug target.

Conclusions

In summary, we have employed membrane-enabled constant-pH MD simulations to investigate the conformational transition of BM2 over a broad pH range. Aligning with prior experiments, BM2 activates with the triple-protonation of His19, but activation is shifted to lower pH values compared to influenza AM2, which can be attributed to electrostatic repulsion between His19 and the early protonated His27. Importantly, we identified the essential role of His27 in the pre-activation hydration of the CT-portion of the channel, which provides an atomic-level explanation for BM2's symmetric H^+ conduction. In addition, we observed that the lipid composition has a significant impact on the BM2 conformational dynamics, favoring the rigid scissor motion upon activation in membranes with reduced fluidity. This work therefore yields new insight into BM2 activation and paves the way for in-depth explicit proton transport modeling of the PT process, as well as possible target identification for drug design.

Experimental procedures

We performed membrane-enabled (50) hybrid-solvent (79) CpHMD simulations on a closed ssNMR structure (PDB ID: 6PVR (38)) using the CHARMM program (92). Consistent with our influenza AM2 studies (13-16, 67), a POPC membrane was used. All simulations used the CHARMM22/CMAP (93-95) force field, the CHARMM36 model (96-98), the CHARMM-modified (89) TIP3P model (88), and the Beglov and Roux's Lennard-Jones model (99) with NBFIX terms (100, 101) to represent the proteins, lipids, waters, and ions, respectively. Systems were stepwise equilibrated following an established protocol (102, 103). In the production run, the pH-based replica exchange protocol (79) was employed to speed up the sampling of BM2 conformations and the protonation states of Glu3, His19, and His27. A total of 15 replicas, ranging from pH 2.5 to 9.5, were run under 308.15 K and 1 atmosphere pressure for 100 ns each, resulting in an aggregate sampling time of 1.5 μs. The simulation of the H27A mutant was also initiated from the closed structure. Details of simulation settings and analysis protocols can be found in the Supporting Information.

Data availability

All data required for the conclusions made here are contained in the article or Supporting Information. Any other data is available at request from the authors.

Supporting information—This article contains supporting information (104-137).

Acknowledgements—The computational resources were provided by The University of Chicago Research Computing Center (RCC).

Author contributions—Z. Y. and G. A. V. designed research. Z. Y., D. T., and Z. W. performed simulations. Z. Y. and J. W. analyzed data. Z. Y. and G. A. V. wrote the manuscript.

Funding and additional information—This research was supported in part by the National Institute of General Medical Sciences (NIGMS) of the National Institutes of Health (NIH) through grant R01GM053148 to G.A.V. The content is solely the responsibility of the authors and does not

necessarily represent the official views of the National Institutes of Health. The research was also supported in part by the Office of Naval Research (Award N00014-21-1-2157 to G.A.V.).

Conflict of interest— The authors declare that they have no conflicts of interest with the contents of this article.

Abbreviations—The abbreviations used are: BM2, influenza B M2 proton channel; AM2, influenza A M2 proton channel; NT, N-terminal; CT, C-terminal; FPS, fixed-protonation-state molecular dynamics; CpHMD, continuous constant-pH molecular dynamics; PT, proton transport; MS-RMD, multiscale reactive molecular dynamics; QM/MM, quantum mechanics/molecular mechanics; HBond, hydrogen-bond; GB, generalized-Born; WT, wildtype; ssNMR, solid-state NMR; POPC, 1-palmitoyl-2-oleoyl-*sn*-glycero-3-phosphocholine; VM+, virus-mimetic; RMSD, root-mean-squared deviation; POPE, 1-palmitoyl-2-oleoyl-*sn*-glycero-3-phosphoethanolamine.

References

1. Hall, E. (2021) Chapter 12: Influenza. In *Epidemiology and Prevention of Vaccine-Preventable Diseases*, 14th Ed. Hall E, Wodi AP, Hamborsky J, Morelli V, Schillie S, eds. Public Health Foundation, Washington, D.C., USA
2. Javanian, M., Barary, M., Ghebrehewet, S., Koppolu, V., Vasigala, V., and Ebrahimpour, S. (2021) A brief review of influenza virus infection. *J. Med. Virol.* **93**, 4638–4646
3. Gonzalez, M. E., and Carrasco, L. (2003) Viroporins. *FEBS Lett.* **552**, 28–34
4. Nieva, J. L., Madan, V., and Carrasco, L. (2012) Viroporins: structure and biological functions. *Nat. Rev. Microbiol.* **10**, 563–574
5. Scott, C., and Griffin, S. (2015) Viroporins: structure, function and potential as antiviral targets. *J. Gen. Virol.* **96**, 2000–2027
6. Lamb, R. A., and Choppin, P. W. (1981) Identification of a Second Protein (M_2) Encoded by RNA Segment 7 of Influenza Virus. *Virology* **112**, 729–737
7. Horvath, C. M., Williams, M. A., and Lamb, R. A. (1990) Eukaryotic coupled translation of tandem cistrons: identification of the influenza B virus BM2 polypeptide. *EMBO J.* **9**, 2639–2647
8. Chizhmakov, I. V., Geraghty, F. M., Ogden, D. C., Hayhurst, A., Antoniou, M., and Hay, A. J. (1996) Selective proton permeability and pH regulation of the influenza virus M2 channel expressed in mouse erythroleukaemia cells. *J. Physiol.* **494**, 329–336
9. Shimbo, K., Brassard, D. L., Lamb, R. A., and Pinto, L. H. (1996) Ion Selectivity and Activation of the M_2 Ion Channel of Influenza Virus. *Biophys. J.* **70**, 1335–1346
10. Mould, J. A., Drury, J. E., Frings, S. M., Kaupp, U. B., Pekosz, A., Lamb, R. A., and Pinto, L. H. (2000) Permeation and Activation of the M_2 Ion Channel of Influenza A Virus. *J. Biol. Chem.* **275**, 31038–31050
11. Lin, T.-I., and Schroeder, C. (2001) Definitive Assignment of Proton Selectivity and Attoampere Unitary Current to the M2 Ion Channel Protein of Influenza A Virus. *J. Virol.* **75**, 3647–3656
12. Mould, J. A., Paterson, R. G., Takeda, M., Ohigashi, Y., Venkataraman, P., Lamb, R. A., and Pinto, L. H. (2003) Influenza B Virus BM2 Protein Has Ion Channel Activity that Conducts Protons across Membranes. *Dev. Cell* **5**, 175–184
13. Liang, R., Li, H., Swanson, J. M. J., and Voth, G. A. (2014) Multiscale simulation reveals a multifaceted mechanism of proton permeation through the influenza A M2 proton channel. *Proc. Natl. Acad. Sci. U.S.A.* **111**, 9396–9401
14. Liang, R., Swanson, J. M. J., Madsen, J. J., Hong, M., DeGrado, W. F., and Voth, G. A. (2016) Acid activation mechanism of the influenza A M2 proton channel. *Proc. Natl. Acad. Sci. U.S.A.* **113**, E6955–E6964
15. Watkins, L. C., Liang, R., Swanson, J. M. J., DeGrado, W. F., and Voth, G. A. (2019) Proton-Induced Conformational and Hydration Dynamics in the Influenza A M2 Channel. *J. Am. Chem. Soc.* **141**, 11667–11676
16. Watkins, L. C., DeGrado, W. F., and Voth, G. A. (2020) Influenza A M2 Inhibitor Binding Understood through Mechanisms of Excess Proton Stabilization and Channel Dynamics. *J. Am. Chem. Soc.* **142**, 17425–17433
17. Pinto, L. H., Holsinger, L. J., and Lamb, R. A. (1992) Influenza Virus M_2 Protein Has Ion Channel Activity. *Cell* **69**, 517–528
18. Takeda, M., Pekosz, A., Shuck, K., Pinto, L. H., and Lamb, R. A. (2002) Influenza A Virus M_2 Ion Channel Activity Is Essential for Efficient Replication in Tissue Culture. *J. Virol.* **76**, 1391–1399
19. Imai, M., Watanabe, S., Ninomiya, A., Obuchi, M., and Odagiri, T. (2004) Influenza B Virus BM2 Protein Is a Crucial Component for Incorporation of Viral Ribonucleoprotein Complex into Virions during Virus Assembly. *J. Virol.* **78**, 11007–11015

20. Hatta, M., Goto, H., and Kawaoka, Y. (2004) Influenza B Virus Requires BM2 Protein for Replication. *J. Virol.* **78**, 5576–5583
21. Pinto, L. H., and Lamb, R. A. (2006) The M2 Proton Channels of Influenza A and B Viruses. *J. Biol. Chem.* **281**, 8997–9000
22. Pielak, R. M., and Chou, J. J. (2011) Influenza M2 proton channels. *Biochim. Biophys. Acta* **1808**, 522–529
23. Sugrue, R. J., and Hay, A. J. (1991) Structural Characteristics of the M2 Protein of Influenza A Viruses: Evidence That It Forms a Tetrameric Channe. *Virology* **180**, 617–624
24. Balannik, V., Lamb, R. A., and Pinto, L. H. (2008) The Oligomeric State of the Active BM2 Ion Channel Protein of Influenza B Virus. *J. Biol. Chem.* **283**, 4895–4904
25. Lamb, R. A., Zebedee, S. L., and Richardson, C. D. (1985) Influenza Virus M_2 Protein Is an Integral Membrane Protein Expressed on the Infected-Cell Surface. *Cell* **40**, 627–633
26. Paterson, R. G., Takeda, M., Ohigashi, Y., Pinto, L. H., and Lamb, R. A. (2003) Influenza B virus BM2 protein is an oligomeric integral membrane protein expressed at the cell surface. *Virology* **306**, 7–17
27. Hong, M., and DeGrado, W. F. (2012) Structural basis for proton conduction and inhibition by the influenza M2 protein. *Protein Sci.* **21**, 1620–1633
28. Schnell, J. R., and Chou, J. J. (2008) Structure and mechanism of the M2 proton channel of influenza A virus. *Nature* **451**, 591–595
29. Acharya, R., Carnevale, V., Fiorin, G., Levine, B. G., Polishchuk, A. L., Balannik, V. *et al.* (2010) Structure and mechanism of proton transport through the transmembrane tetrameric M2 protein bundle of the influenza A virus. *Proc. Natl. Acad. Sci. U.S.A.* **107**, 15075–15080
30. Sansom, M. S. P., Kerr, I. D., Smith, G. R., and Son, H. S. (1997) The Influenza A Virus M2 Channel: A Molecular Modeling and Simulation Study. *Virology* **233**, 163–173
31. Schweighofer, K. J., and Pohorille, A. (2000) Computer Simulation of Ion Channel Gating: The M_2 Channel of Influenza A Virus in a Lipid Bilayer. *Biophys. J.* **78**, 150–163
32. Khurana, E., Peraro, M. D., DeVane, R., Vemparala, S., DeGrado, W. F., and Klein, M. L. (2009) Molecular dynamics calculations suggest a conduction mechanism for the M2 proton channel from influenza A virus. *Proc. Natl. Acad. Sci. U.S.A.* **106**, 1069–1074
33. Phongphanphanee, S., Rungrotmongkol, T., Yoshida, N., Hannongbua, S., and Hirata, F. (2010) Proton Transport through the Influenza A M2 Channel: Three-Dimensional Reference Interaction Site Model Study. *J. Am. Chem. Soc.* **132**, 9782–9788
34. Gu, R.-X., Liu, L. A., Wang, Y.-H., Xu, Q., and Wei, D.-Q. (2013) Structural Comparison of the Wild-Type and Drug-Resistant Mutants of the Influenza A M2 Proton Channel by Molecular Dynamics Simulations. *J. Phys. Chem. B* **117**, 6042–6051
35. Thomaston, J. L., Alfonso-Prieto, M., Woldeyes, R. A., Fraser, J. S., Klein, M. L., Fiorin, G., and DeGrado, W. F. (2015) High-resolution structures of the M2 channel from influenza A virus reveal dynamic pathways for proton stabilization and transduction. *Proc. Natl. Acad. Sci. U.S.A.* **112**, 14260–14265
36. Gelenter, M. D., Mandala, V. S., Niesen, M. J. M., Sharon, D. A., Dregni, A. J., Willard, A. P., and Hong, M. (2021) Water orientation and dynamics in the closed and open influenza B virus M2 proton channels. *Commun. Biol.* **4**, 338
37. Sharma, M., Yi, M., Dong, H., Qin, H., Peterson, E., Busath, D. D. *et al.* (2010) Insight into the Mechanism of the Influenza A Proton Channel from a Structure in a Lipid Bilayer. *Science* **330**, 509–512
38. Mandala, V. S., Loftis, A. R., Shcherbakov, A. A., Pentelute, B. L., and Hong, M. (2020) Atomic structures of closed and open influenza B M2 proton channel reveal the conduction mechanism. *Nat. Struct. Mol. Biol.* **27**, 160–167
39. Smart, O. S., Neduvelil, J. G., Wang, X., Wallace, B. A., and Sansom, M. S. P. (1996) HOLE: A program for the analysis of the pore dimensions of ion channel structural models. *J. Mol. Graph.* **14**, 354−360
40. Lomize, A. L., Pogozheva, I. D., Lomize, M. A., and Mosberg, H. I. (2006) Positioning of proteins in membranes: A computational approach. *Protein Sci.* **15**, 1318−1333
41. Altschul, S. F., Gish, W., Miller, W., Myers, E. W., and Lipman, D. J. (1990) Basic Local Alignment Search Tool. *J. Mol. Biol.* **215**, 403–410
42. Wang, C., Lamb, R. A., and Pinto, L. H. (1995) Activation of the M_2 Ion Channel of Influenza Virus: A Role for the Transmembrane Domain Histidine Residue. *Biophys. J.* **69**, 1363–1371
43. Venkataraman, P., Lamb, R. A., and Pinto, L. H. (2005) Chemical Rescue of Histidine Selectivity Filter Mutants of the M2 Ion Channel of Influenza A Virus. *J. Biol. Chem.* **280**, 21463–21472
44. Pielak, R. M., and Chou, J. J. (2010) Kinetic Analysis of the M2 Proton Conduction of the Influenza Virus. *J. Am. Chem. Soc.* **132**, 17695–17697
45. Hu, J., Fu, R., Nishimura, K., Zhang, L., Zhou, H.-X., Busath, D. D. *et al.* (2006) Histidines, heart of the hydrogen ion channel from influenza A virus: Toward an understanding of conductance and proton selectivity. *Proc. Natl. Acad. Sci. U.S.A.* **103**, 6865–6870
46. Hu, F., Schmidt-Rohr, K., and Hong, M. (2012) NMR Detection of pH-Dependent Histidine–Water Proton Exchange Reveals the Conduction Mechanism of a Transmembrane Proton Channel. *J. Am. Chem. Soc.* **134**, 3703–3713

47. Okada, A., Miura, T., and Takeuchi, H. (2001) Protonation of Histidine and Histidine–Tryptophan Interaction in the Activation of the M2 Ion Channel from Influenza A Virus. *Biochemistry* **40**, 6053–6060
48. Pinto, L. H., Dieckmann, G. R., Gandhi, C. S., Papworth, C. G., Braman, J., Shaughnessy, M. A. *et al.* (1997) A functionally defined model for the M_2 proton channel of influenza A virus suggests a mechanism for its ion selectivity. *Proc. Natl. Acad. Sci. U.S.A.* **94**, 11301–11306
49. Hu, F., Luo, W., and Hong, M. (2010) Mechanisms of Proton Conduction and Gating in Influenza M2 Proton Channels from Solid-State NMR. *Science* **330**, 505–508
50. Chen, W., Huang, Y., and Shen, J. (2016) Conformational Activation of a Transmembrane Proton Channel from Constant pH Molecular Dynamics. *J. Phys. Chem. Lett.* **7**, 3961–3966
51. Torabifard, H., Panahi, A., and Brooks III, C. L. (2020) M2 amphipathic helices facilitate pH-dependent conformational transition in influenza A virus. *Proc. Natl. Acad. Sci. U.S.A.* **117**, 3583–3591
52. Hong, M., Fritzsching, K. J., and Williams, J. K. (2012) Hydrogen-Bonding Partner of the Proton-Conducting Histidine in the Influenza M2 Proton Channel Revealed From ^{1}H Chemical Shifts. *J. Am. Chem. Soc.* **134**, 14753–14755
53. Voth, G. A. (2006) Computer Simulation of Proton Solvation and Transport in Aqueous and Biomolecular Systems. *Acc. Chem. Res.* **39**, 143–150
54. Knight, C., and Voth, G. A. (2011) The Curious Case of the Hydrated Proton. *Acc. Chem. Res.* **45**, 101–109
55. Knight, C., Lindberg, G. E., and Voth, G. A. (2012) Multiscale reactive molecular dynamics. *J. Chem. Phys.* **137**, 22A525
56. Kaiser, S., Yue, Z., Peng, Y., Nguyen, T. D., Chen, S., Teng, D., and Voth, G. A. (2024) Molecular Dynamics Simulation of Complex Reactivity with the Rapid Approach for Proton Transport and Other Reactions (RAPTOR) Software Package. *J. Phys. Chem. B* **128**, 4959–4974
57. Warshel, A., and Levitt, M. (1976) Theoretical Studies of Enzymic Reactions: Dielectric, Electrostatic and Steric Stabilization of the Carbonium Ion in the Reaction of Lysozyme. *J. Mol. Biol.* **103**, 227–249
58. Field, M. J., Bash, P. A., and Karplus, M. (1990) A Combined Quantum Mechanical and Molecular Mechanical Potential for Molecular Dynamics Simulations. *J. Comput. Chem.* **11**, 700–733
59. Senn, H. M., and Thiel, W. (2009) QM/MM Methods for Biomolecular Systems. *Angew. Chem. Int. Ed.* **48**, 1198–1229
60. Chizhmakov, I. V., Ogden, D. C., Geraghty, F. M., Hayhurst, A., Skinner, A., Betakova, T., and Hay, A. J. (2003) Differences in conductance of M2 proton channels of two influenza viruses at low and high pH. *J. Physiol.* **546**, 427–438
61. Mould, J. A., Li, H.-C., Dudlak, C. S., Lear, J. D., Pekosz, A., Lamb, R. A., and Pinto, L. H. (2000) Mechanism for Proton Conduction of the M_2 Ion Channel of Influenza A Virus. *J. Biol. Chem.* **275**, 8592–8599
62. Tang, Y., Zaitseva, F., Lamb, R. A., and Pinto, L. H. (2002) The Gate of the Influenza Virus M_2 Proton Channel Is Formed by a Single Tryptophan Residue. *J. Biol. Chem.* **277**, 39880–39886
63. Hay, A. J., Wolstenholme, A. J., Skehel, J. J., and Smith, M. H. (1985) The molecular basis of the specific anti-influenza action of amantadine. *EMBO J.* **4**, 3021–3024
64. Betakova, T., Ciampor, F., and Hay, A. J. (2005) Influence of residue 44 on the activity of the M2 proton channel of influenza A virus. *J. Gen. Virol.* **86**, 181–184
65. Balannik, V., Carnevale, V., Fiorin, G., Levine, B. G., Lamb, R. A., Klein, M. L. *et al.* (2010) Functional Studies and Modeling of Pore-Lining Residue Mutants of the Influenza A Virus M2 Ion Channel. *Biochemistry* **49**, 696–708
66. Ma, C., Fiorin, G., Carnevale, V., Wang, J., Lamb, R. A., Klein, M. L. *et al.* (2013) Asp44 Stabilizes the Trp41 Gate of the M2 Proton Channel of Influenza A Virus. *Structure* **21**, 2033–2041
67. Watkins, L. C., DeGrado, W. F., and Voth, G. A. (2022) Multiscale Simulation of an Influenza A M2 Channel Mutant Reveals Key Features of Its Markedly Different Proton Transport Behavior. *J. Am. Chem. Soc.* **144**, 769–776
68. Ma, C., and Wang, J. (2018) Functional studies reveal the similarities and differences between AM2 and BM2 proton channels from influenza viruses. *Biochim. Biophys. Acta Biomembr.* **1860**, 272–280
69. Wang, J., Pielak, R. M., McClintock, M. A., and Chou, J. J. (2009) Solution structure and functional analysis of the influenza B proton channel. *Nat. Struct. Mol. Biol.* **16**, 1267–1271
70. Ma, C., Soto, C. S., Ohigashi, Y., Taylor, A., Bournas, V., Glawe, B. *et al.* (2008) Identification of the Pore-lining Residues of the BM2 Ion Channel Protein of Influenza B Virus. *J. Biol. Chem.* **283**, 15921–15931
71. Betakova, T., and Hay, A. J. (2009) Comparison of the activities of BM2 protein and its H19 and W23 mutants of influenza B virus with activities of M2 protein and its H37 and W41 mutants of influenza A virus. *Arch. Virol.* **154**, 1619–1624
72. Otomo, K., Toyama, A., Miura, T., and Takeuchi, H. (2009) Interactions Between Histidine and Tryptophan Residues in the BM2 Proton Channel from Influenza B Virus. *J. Biochem.* **145**, 543–554
73. Rouse, S. L., Carpenter, T., Stansfeld, P. J., and Sansom, M. S. P. (2009) Simulations of the BM2 Proton Channel Transmembrane Domain from Influenza Virus B. *Biochemistry* **48**, 9949–9951

74. Zhang, Y., Shen, H., Zhang, M., and Li, G. (2013) Exploring the Proton Conductance and Drug Resistance of BM2 Channel through Molecular Dynamics Simulations and Free Energy Calculations at Different pH Conditions. *J. Phys. Chem. B* **117**, 982–988
75. Chowdhury, U. D., and Bhargava, B. L. (2022) Understanding the conformational changes in the influenza B M2 ion channel at various protonation states. *Biophys. Chem.* **289**, 106859
76. Williams, J. K., Tietze, D., Lee, M., Wang, J., and Hong, M. (2016) Solid-State NMR Investigation of the Conformation, Proton Conduction, and Hydration of the Influenza B Virus M2 Transmembrane Proton Channel. *J. Am. Chem. Soc.* **138**, 8143–8155
77. Williams, J. K., Shcherbakov, A. A., Wang, J., and Hong, M. (2017) Protonation equilibria and pore-opening structure of the dual-histidine influenza B virus M2 transmembrane proton channel from solid-state NMR. *J. Biol. Chem.* **292**, 17876–17884
78. Zhang, Y., Zhang, H., and Zheng, Q. (2019) A unique activation–promotion mechanism of the influenza B M2 proton channel uncovered by multiscale simulations. *Phys. Chem. Chem. Phys.* **21**, 2984–2991
79. Wallace, J. A., and Shen, J. K. (2011) Continuous Constant pH Molecular Dynamics in Explicit Solvent with pH-Based Replica Exchange. *J. Chem. Theory Comput.* **7**, 2617−2629
80. Hill, A. V. (1910) The possible effects of the aggregation of the molecules of haemoglobin on its dissociation curves. *J. Physiol.* **40**, iv−vii
81. Kwon, B., Roos, M., Mandala, V. S., Shcherbakov, A. A., and Hong, M. (2019) Elucidating Relayed Proton Transfer through a His–Trp–His Triad of a Transmembrane Proton Channel by Solid-State NMR. *J. Mol. Biol.* **431**, 2554–2566
82. Wallace, J. A., Wang, Y., Shi, C., Pastoor, K. J., Nguyen, B.-L., Xia, K., and Shen, J. K. (2011) Toward accurate prediction of pK_a values for internal protein residues: The importance of conformational relaxation and desolvation energy. *Proteins* **79**, 3364−3373
83. Luo, W., Cady, S. D., and Hong, M. (2009) Immobilization of the Influenza A M2 Transmembrane Peptide in Virus Envelope–Mimetic Lipid Membranes: A Solid-State NMR Investigation. *Biochemistry* **48**, 6361–6368
84. Perly, B., Smith, I. C., and Jarrell, H. C. (1985) Acyl Chain Dynamics of Phosphatidylethanolamines Containing Oleic Acid and Dihydrosterculic Acid: ^{2}H NMR Relaxation Studies. *Biochemistry* **24**, 4659–4665
85. Huang, C.-h., Li, S., Lin, H.-n., and Wang, G. (1996) On the Bilayer Phase Transition Temperatures for Monoenoic Phosphatidylcholines and Phosphatidylethanolamines and the Interconversion between Them. *Arch. Biochem. Biophys.* **334**, 135–142
86. Shaikh, S. R., Brzustowicz, M. R., Gustafson, N., Stillwell, W., and Wassall, S. R. (2002) Monounsaturated PE Does not Phase-Separate from the Lipid Raft Molecules Sphingomyelin and Cholesterol: Role for Polyunsaturation? *Biochemistry* **41**, 10593–105602
87. Shalaev, E. Y., and Steponkus, P. L. (2003) Glass Transition of a Synthetic Phospholipid in the Lamellar Phase. *J. Phys. Chem. B* **107**, 8734–8737
88. Jorgensen, W. L., Chandrasekhar, J., Madura, J. D., Impey, R. W., and Klein, M. L. (1983) Comparison of simple potential functions for simulating liquid water. *J. Chem. Phys.* **79**, 926−935
89. Durell, S. R., Brooks, B. R., and Ben-Naim, A. (1994) Solvent-Induced Forces between Two Hydrophilic Groups. *J. Phys. Chem.* **98**, 2198−2202
90. Vega, C., Sanz, E., and Abascal, J. L. (2005) The melting temperature of the most common models of water. *J. Chem. Phys.* **122**, 114507
91. Stouffer, A. L., Acharya, R., Salom, D., Levine, A. S., Di Costanzo, L., Soto, C. S. *et al.* (2008) Structural basis for the function and inhibition of an influenza virus proton channel. *Nature* **451**, 596–599
92. Brooks, B. R., Brooks III, C. L., Mackerell Jr., A. D., Nilsson, L., Petrella, R. J., Roux, B. *et al.* (2009) CHARMM: The Biomolecular Simulation Program. *J. Comput. Chem.* **30**, 1545−1614
93. MacKerell Jr., A. D., Bashford, D., Bellott, M., Dunbrack Jr., R. L., Evanseck, J. D., Field, M. J. *et al.* (1998) All-Atom Empirical Potential for Molecular Modeling and Dynamics Studies of Proteins. *J. Phys. Chem. B* **102**, 3586−3616
94. Mackerell Jr., A. D., Feig, M., and Brooks III, C. L. (2004) Extending the Treatment of Backbone Energetics in Protein Force Fields: Limitations of Gas-Phase Quantum Mechanics in Reproducing Protein Conformational Distributions in Molecular Dynamics Simulations. *J. Comput. Chem.* **25**, 1400−1415
95. MacKerell Jr., A. D., Feig, M., and Brooks III, C. L. (2004) Improved Treatment of the Protein Backbone in Empirical Force Fields. *J. Am. Chem. Soc.* **126**, 698−699
96. Klauda, J. B., Venable, R. M., Freites, J. A., O'Connor, J. W., Tobias, D. J., Mondragon-Ramirez, C. *et al.* (2010) Update of the CHARMM All-Atom Additive Force Field for Lipids: Validation on Six Lipid Types. *J. Phys. Chem. B* **114**, 7830−7843
97. Lim, J. B., Rogaski, B., and Klauda, J. B. (2012) Update of the Cholesterol Force Field Parameters in CHARMM. *J. Phys. Chem. B* **116**, 203–210
98. Venable, R. M., Sodt, A. J., Rogaski, B., Rui, H., Hatcher, E., MacKerell Jr., A. D. *et al.* (2014) CHARMM All-Atom Additive Force Field for Sphingomyelin: Elucidation of Hydrogen Bonding and of Positive Curvature. *Biophys J* **107**, 134–145

99. Beglov, D., and Roux, B. (1994) Finite representation of an infinite bulk system: Solvent boundary potential for computer simulations. *J. Chem. Phys.* **100**, 9050−9063
100. Luo, Y., and Roux, B. (2010) Simulation of Osmotic Pressure in Concentrated Aqueous Salt Solutions. *J. Phys. Chem. Lett.* **1**, 183−189
101. Venable, R. M., Luo, Y., Gawrisch, K., Roux, B., and Pastor, R. W. (2013) Simulations of Anionic Lipid Membranes: Development of Interaction-Specific Ion Parameters and Validation Using NMR Data. *J. Phys. Chem. B* **117**, 10183−10192
102. Yue, Z., Chen, W., Zgurskaya, H. I., and Shen, J. (2017) Constant pH Molecular Dynamics Reveals How Proton Release Drives the Conformational Transition of a Transmembrane Efflux Pump. *J. Chem. Theory Comput.* **13**, 6405−6414
103. Yue, Z., Li, C., Voth, G. A., and Swanson, J. M. J. (2019) Dynamic Protonation Dramatically Affects the Membrane Permeability of Drug-like Molecules. *J. Am. Chem. Soc.* **141**, 13421−13433
104. Lomize, M. A., Pogozheva, I. D., Joo, H., Mosberg, H. I., and Lomize, A. L. (2012) OPM database and PPM web server: resources for positioning of proteins in membranes. *Nucleic Acids Res.* **40**, D370−D376
105. Jo, S., Kim, T., and Im, W. (2007) Automated Builder and Database of Protein/Membrane Complexes for Molecular Dynamics Simulations. *PLoS ONE* **2**, e880
106. Wu, E. L., Cheng, X., Jo, S., Rui, H., Song, K. C., Dávila-Contreras, E. M. *et al.* (2014) CHARMM-GUI *Membrane Builder* Toward Realistic Biological Membrane Simulations. *J. Comput. Chem.* **35**, 1997−2004
107. Brünger, A. T., and Karplus, M. (1988) Polar Hydrogen Positions in Proteins: Empirical Energy Placement and Neutron Diffraction Comparison. *Proteins* **4**, 148−156
108. Levitt, M., and Lifson, S. (1969) Refinement of Protein Conformations using a Macromolecular Energy Minimization Procedure. *J. Mol. Biol.* **46**, 269−279
109. Brooks, B. R., Bruccoleri, R. E., Olafson, B. D., States, D. J., Swaminathan, S., and Karplus, M. (1983) CHARMM: A Program for Macromolecular Energy, Minimization, and Dynamics Calculations. *J. Comput. Chem.* **4**, 187−217
110. Im, W., Lee, M. S., and Brooks III, C. L. (2003) Generalized Born Model with a Simple Smoothing Function. *J. Comput. Chem.* **24**, 1691−1702
111. Chen, J., Im, W., and Brooks III, C. L. (2006) Balancing Solvation and Intramolecular Interactions: Toward a Consistent Generalized Born Force Field. *J. Am. Chem. Soc.* **128**, 3728−3736
112. Abraham, M. J., Murtola, T., Schulz, R., Páll, S., Smith, J. C., Hess, B., and Lindahl, E. (2015) GROMACS: High performance molecular simulations through multi-level parallelism from laptops to supercomputers. *SoftwareX* **1−2**, 19−25
113. Avanti® Polar Lipids. Products: 860061 | Egg SM
114. Kutzner, C., Páll, S., Fechner, M., Esztermann, A., de Groot, B. L., and Grubmüller, H. (2015) Best Bang for Your Buck: GPU Nodes for GROMACS Biomolecular Simulations. *J. Comput. Chem.* **36**, 1990−2008
115. Kutzner, C., Páll, S., Fechner, M., Esztermann, A., Groot, B. L., and Grubmüller, H. (2019) More Bang for Your Buck: Improved use of GPU Nodes for GROMACS 2018. *J. Comput. Chem.* **40**, 2418−2431
116. Hockney, R. W. (1970) The Potential Calculation and Some Applications. *Methods Comput. Phys.* **9**, 135−211
117. Swope, W. C., Andersen, H. C., Berens, P. H., and Wilson, K. R. (1982) A computer simulation method for the calculation of equilibrium constants for the formation of physical clusters of molecules: Application to small water clusters. *J. Chem. Phys.* **76**, 637−649
118. Ryckaert, J.-P., Ciccotti, G., and Berendsen, H. J. C. (1977) Numerical Integration of the Cartesian Equations of Motion of a System with Constraints: Molecular Dynamics of *n*-Alkanes. *J. Comput. Phys.* **23**, 327−341
119. Hess, B., Bekker, H., Berendsen, H. J. C., and Fraaije, J. G. E. M. (1997) LINCS: A Linear Constraint Solver for Molecular Simulations. *J. Comput. Chem.* **18**, 1463−1472
120. Steinbach, P. J., and Brooks, B. R. (1994) New Spherical-Cutoff Methods for Long-Range Forces in Macromolecular Simulation. *J. Comput. Chem.* **15**, 667−683
121. Darden, T., York, D., and Pedersen, L. (1993) Particle mesh Ewald: An $N\bullet\log(N)$ method for Ewald sums in large systems. *J. Chem. Phys.* **98**, 10089−10092
122. Essmann, U., Perera, L., Berkowitz, M. L., Darden, T., Lee, H., and Pedersen, L. G. (1995) A smooth particle mesh Ewald method. *J. Chem. Phys.* **103**, 8577−8593
123. Nosé, S. (1984) A molecular dynamics method for simulations in the canonical ensemble. *Mol. Phys.* **52**, 255−268
124. Hoover, W. G. (1985) Canonical dynamics: Equilibrium phase-space distributions. *Phys. Rev. A* **31**, 1695−1697
125. Feller, S. E., Zhang, Y., Pastor, R. W., and Brooks, B. R. (1995) Constant pressure molecular dynamics simulation: The Langevin piston method. *J. Chem. Phys.* **103**, 4613−4621
126. Parrinello, M., and Rahman, A. (1981) Polymorphic transitions in single crystals: A new molecular dynamics method. *J. Appl. Phys.* **52**, 7182−7190
127. Lee, J., Cheng, X., Swails, J. M., Yeom, M. S., Eastman, P. K., Lemkul, J. A. *et al.* (2016) CHARMM-GUI Input Generator for NAMD, GROMACS, AMBER, OpenMM, and CHARMM/OpenMM Simulations Using the CHARMM36 Additive Force Field. *J. Chem. Theory Comput.* **12**, 405−413

128. Loncharich, R. J., Brooks, B. R., and Pastor, R. W. (1992) Langevin Dynamics of Peptides: The Frictional Dependence of Isomerization Rates of *N*-Acetylalanyl-*N'*-Methylamide. *Biopolymers* **32**, 523−535
129. Im, W., Feig, M., and Brooks III, C. L. (2003) An Implicit Membrane Generalized Born Theory for the Study of Structure, Stability, and Interactions of Membrane Proteins. *Biophys. J.* **85**, 2900−2918
130. Srinivasan, J., Trevathan, M. W., Beroza, P., and Case, D. A. (1999) Application of a pairwise generalized Born model to proteins and nucleic acids: inclusion of salt effects. *Theor. Chem. Acc.* **101**, 426−434
131. Metropolis, N., and Ulam, S. (1949) The Monte Carlo Method. *J. Am. Stat. Assoc.* **44**, 335−341
132. Yue, Z., Li, C., and Voth, G. A. (2023) The role of conformational change and key glutamic acid residues in the ClC-ec1 antiporter. *Biophys. J.* **122**, 1068–1085
133. Khandogin, J., and Brooks III, C. L. (2005) Constant pH Molecular Dynamics with Proton Tautomerism. *Biophys. J.* **89**, 141−157
134. de Grotthuss, C. J. T. (1806) Sur la décomposition de l'eau et des corps qu'elle tient en dissolution à l'aide de l'électricité galvanique. *Ann. Chim.* **58**, 54−74
135. Michaud-Agrawal, N., Denning, E. J., Woolf, T. B., and Beckstein, O. (2011) MDAnalysis: A Toolkit for the Analysis of Molecular Dynamics Simulations. *J. Comput. Chem.* **32**, 2319–2327
136. Humphrey, W., Dalke, A., and Schulten, K. (1996) VMD: Visual Molecular Dynamics. *J. Mol. Graph.* **14**, 33−38
137. Grace Development Team. (2015) Grace version 5.1.25. https://plasma-gate.weizmann.ac.il/Grace